PAPER

Check for updates

Electrochemical reactivity of graphene under mechanical strain†

Hyo Jin Lee,[a] Jinhyun Hwang,[b] Hyo Chan Hong,[a] Young Wook Hwang,[a] Jiyeon Lee,[b] Gaeun Cho,[a] Dalsu Choi,[a] Kilwon Cho [ID] *[b] and Hyo Chan Lee [ID] *[a]

The electrochemical reaction of graphene with aryl diazonium molecules is recognized as an effective method for surface functionalization of graphene. As the charge-transfer rate between graphene and the diazonium molecules determines the degree of functionalization, considerable research has been dedicated to understanding the factors that influence this metric. Among them, the mechanical strain in graphene is particularly crucial because mechanical deformation is inevitable in flexible devices. The mechanical strain in graphene is predicted to generate a pseudo-scalar potential that shifts the energy of the Dirac point, but its influence on the electrochemical reactivity of graphene has been largely overlooked. In this study, we investigate the effect of mechanical strain on the electrochemical reactivity of graphene with 4-nitrobenzenediazonium tetrafluoroborate using a combination of experimental techniques and theoretical modeling. Our results reveal that the electrochemical reactivity of graphene initially decreases with strain but increases as the strain continues to increase. This behavior is explained by the Marcus–Gerischer theory, which accounts for the strain-induced shifts in the electronic density of states of graphene and the resulting changes in the electron transfer rate.

1. Introduction

Graphene-based biosensors possess significant application potential in next-generation medicine owing to their ability to detect target molecules rapidly and effectively.[1–9] The high specific surface area and charge carrier mobility of graphene enhances signal transduction events, resulting in superior sensitivity.[10–15] However, despite this high sensitivity, challenges concerning stability and reproducibility persist. To address these challenges, researchers have focused on the functionalization of graphene surfaces to ensure the stable attachment of ligands that detect target molecules.[16–21] Among various functionalization strategies available, aryl diazonium chemistry is notable for its ease of preparation and ability to form strong covalent bonds with graphene, leading to stable surface modification.[22–28]

Aryl diazonium chemistry involves the transfer of charge from graphene to aryl diazonium cations, leading to the generation of aryl radicals and the subsequent formation of covalent bonds with graphene.[29–36] As the charge-transfer rate from graphene to the diazonium molecules governs the degree of functionalization, significant efforts have been made to

understand the factors that influence this metric within the framework of the Marcus–Gerischer theory. Park *et al.* demonstrated the effect of doping on the electrochemical reactivity of graphene using the Marcus–Gerischer theory.[37] By transferring graphene onto a self-assembled monolayer (SAM), they induced n-doping of graphene, which subsequently resulted in a higher charge-transfer rate. Wang *et al.* analyzed the impact of the electron–hole puddle amplitude induced by the substrates.[38] The results revealed that although the region is predominantly p-doped on average, the presence of localized n-doped puddles within contributes to the reactivity. The number of graphene layers and their stacking configurations also affect the electrochemical reactivity.[39,40]

In addition to the doping level and amplitude of electron–hole puddles, the strain in graphene is another promising factor that can influence its electrochemical reactivity, especially in flexible devices where mechanical deformation is inevitable. Strain in graphene alters its electronic structure and is predicted to generate a pseudo-scalar potential that shifts the energy of the Dirac point.[41–43] Consequently, the work function of graphene increases by 0.025–0.04 eV for every 1% of tensile strain applied. According to the Marcus–Gerischer theory, changes in the electronic structure of graphene directly impact the rate of charge transfer between graphene and redox systems, such as those involving redox biomolecules or electrochemical reactions. This unique property suggests that the strain plays a critical role in determining the electrochemical reactivity of graphene with diazonium molecules. However, only a limited

[a]Department of Chemical Engineering, Myongji University, Yongin, 17058, Republic of Korea. E-mail: hyochan@mju.ac.kr

[b]Department of Chemical Engineering, Pohang University of Science and Technology, Pohang, 37673, Republic of Korea. E-mail: kwcho@postech.ac.kr

† Electronic supplementary information (ESI) available. See DOI: https://doi.org/10.1039/d5ta02062j

23696 | *J. Mater. Chem. A*, 2025, **13**, 23696–23705

This journal is © The Royal Society of Chemistry 2025

number of studies have investigated the influence of strain as a factor that modulates the electrochemical reactivity of graphene.[44–47] A comprehensive understanding of this behavior has remained elusive.

In this study, we explored the effect of tensile strain on the electrochemical reactivity of graphene. To achieve this, graphene samples with varying levels of tensile strain were prepared by transferring graphene onto silica nanosphere (NS) arrays. The electrochemical reactivity of these samples was assessed by observing their reaction with 4-nitro-benzenediazonium (4-NBD) tetrafluoroborate as a function of the applied tensile strain. Furthermore, we introduce a modified Marcus–Gerischer theory that accounts for the strain-induced shift in the energy of the graphene Dirac point. This theoretical framework successfully predicts our experimental findings, suggesting that the strain-induced pseudo-scalar potentials in graphene may be responsible for the observed effects of strain on its electrochemical reactivity.

2. Methods

2.1. Synthesis and transfer of graphene samples

Single-layer graphene was grown on a Cu foil substrate using CVD. Initially, the Cu foil was annealed in a hydrogen atmosphere (1000 °C, 50 sccm) for 30 min. The hydrogen flow was then reduced, and graphene growth was carried out with methane for 15 min (1000 °C, 30 sccm methane, and 5 sccm hydrogen). After growth, the graphene on the Cu foil was coated with polymethyl methacrylate (PMMA) *via* spin coating (3000 rpm, 1 min). PMMA/graphene/copper was floated on an ammonium persulfate (APS) solution (50 mM APS in water) for over 4 h to etch away the copper. The samples were transferred to water for 5 min to remove the residual APS. To prepare chemically doped graphene, the sample was floated on a TFSA solution (10 mL of 20 mM TFSA in nitromethane and 100 mL of DI water) for 5 min. The graphene was then transferred onto the NS substrate. The sample was dried under ambient conditions for at least 12 h and later under vacuum conditions (40 °C, ~0.1 bar) for 12 h. The samples were then immersed in acetone for 30 min to remove PMMA layers.

2.2. DFT calculations

DFT calculations were conducted at the generalized gradient approximation (GGA) level using the Perdew–Burke–Ernzerhof (PBE) exchange-correlation functional, as implemented in the CASTEP module in Materials Studio 2020. To accurately account for van der Waals interactions, which are crucial for adsorption processes, a dispersion correction was applied to the PBE functional, following the method proposed by Tkatchenko and Scheffler (DFT-TS). Ultrasoft pseudopotentials were employed throughout the study to represent core electrons, whereas valence electrons were treated explicitly. The geometries of both graphene and 4-NBD were individually optimized using a vacuum slab of 20 Å thickness to prevent any spurious interactions between the periodic images. The optimization was performed until the energy converged within 1×10^{-5} eV per

atom, with a force threshold of 0.03 eV Å^{-1} and a displacement convergence of 0.001 Å. The energy cutoff for the plane-wave basis set was set to 630 eV and a $1 \times 1 \times 1$ k-point mesh was employed for the slab calculations.

3. Results and discussion

3.1. Preparation of graphene on the NS array

Fig. 1a presents a schematic of the experimental process for evaluating the electrochemical reactivity of the tensile-strained graphene. Silica NSs with a diameter of 500 nm were dispersed in deionized (DI) water and spin-coated onto 300 nm-thick SiO_2/Si wafers. Fig. 1b shows a scanning electron microscopy (SEM) image of graphene on the NS array. The spin-coating process led to the self-assembly of the NSs into a monolayer array with a hexagonal close-packed structure. This monolayer NS array formed clusters ranging from several tens to hundreds of micrometers in size. Subsequently, graphene synthesized *via* chemical vapor deposition (CVD) was wet-transferred onto the NS-coated substrate (G/NS). Using this strategy, significant tensile strain, on the order of a few percent, can be applied locally to graphene without changing its doping level.[48–50]

The atomic force microscopy (AFM) image in Fig. 1c illustrates the topography of the G/NS sample, revealing apex regions where graphene is in direct contact with the NSs, as well as free-standing areas where graphene is not attached to the NSs. The latter regions are surrounded by distinctive wrinkles that connect adjacent NSs, suggesting a significant radial tensile strain in the graphene at the apex of the NSs.[51] To further confirm the presence
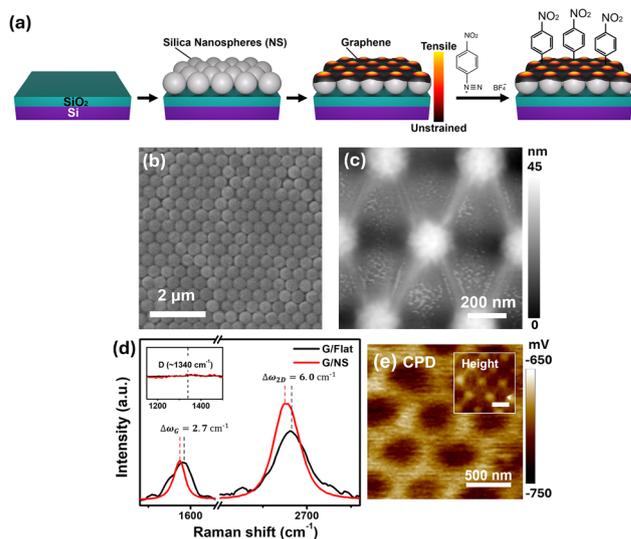

Fig. 1 Preparation of strained graphene samples. (a) Experimental scheme illustrating the transfer of graphene onto substrates coated with 500 nm silica NSs, followed by covalent chemical functionalization with 4-NBD. (b) SEM and (c) AFM images showing graphene after transfer onto the NS. (d) Raman spectra of graphene on flat substrates (G/Flat) and on NS substrates (G/NS). Inset: D-band spectra of graphene films on flat and NS substrates before functionalization with diazonium salts. (e) CPD image of the G/NS. Inset: Height image of the same region.

of tensile strain in the graphene on the NS arrays, we compared the Raman spectra of G/NS with those of graphene on flat SiO_2 substrates (G/Flat) (Fig. 1d). Both spectra exhibited the characteristic peaks of graphene: G (1580–1590 cm^{-1}) and 2D (2660–2680 cm^{-1}). The corresponding intensity ratio between the peaks, (I_{2D}/I_G), was at least 1.7. This indicated that the graphene was a monolayer. Additionally, the D peak was nearly absent in both the G/flat and G/NS samples, demonstrating negligible defect density in graphene. Thus, defects can be ruled out as a contributing factor affecting the electrochemical reactivity observed in the G/Flat and G/NS samples. Notably, compared to G/flat, G/NS exhibited redshifts in both the G and 2D peaks. The positions of the 2D and G peaks in graphene were affected by both strain and doping.[52] The ratio of the shift in the 2D peak to that in the G peak ($\Delta\omega_{2D}/\Delta\omega_G$) in G/NS relative to G/flat was approximately 2.3, suggesting that both samples had similar doping levels and that the NS array effectively applied tensile strain onto the graphene (Fig. S1†).[53,54] This, in turn, implies that the graphene regions directly attached to the NSs, as well as the free-standing regions had similar doping levels, which was consistent with previous reports.[55] To investigate the spatial strain distribution in G/NS, we employed Kelvin Probe Force Microscopy (KPFM) to map local variations in the surface potential (Fig. 1e). KPFM measures the contact potential difference (CPD) between the n-doped Si tip and the sample, which is defined as CPD $= (\varphi_{tip} - \varphi_{sample})/e$ where φ_{tip} represents the work function of the n-doped Si tips (approximately 4.1 eV), φ_{sample} is the work function of graphene, and e is the elementary charge. In our experimental configuration, a greater negative CPD value indicates a larger graphene work function. Given the influence of doping from the underlying NS array is negligible (Fig. 1d), the observed variations in the work function of graphene primarily arise from the spatially varying strains and the associated pseudo-electric fields. When local tensile strain is applied, the entire band structure of graphene in the strained region shifts downward relative to the vacuum level (E_{vac}). Electrons consequently flow from unstrained regions into strained regions until a uniform Fermi level (E_F) is re-established. The resulting charge imbalance creates an in-plane electric field that elevates the local vacuum level in the strained areas. Thus, the work function $\varphi_{sample} = E_{vac} - E_F$ is higher at the apex regions (Fig. S2†). Accordingly, CPD mapping demonstrates tensile strain in graphene is localized to the apices of the nanospheres. Although the spatial resolution of KPFM is constrained by the geometry of the tip and cantilever, the technique offers valuable qualitative insights into relative local work function variations, thereby highlighting the distribution of strain across the graphene surface.

Finally, to characterize the electrochemical reactivity of the tensile-strained graphene, the sample was subjected to a reaction with 4-NBD. Graphene samples on the NS array were immersed in a 10 mM aqueous solution of 4-NBD with constant stirring at 35 °C for 300 s. After the reaction, the sample was rinsed with DI water to remove residual reactants. Through this process, a delocalized electron is transferred from the graphene to the diazonium cation, rapidly forming an aryl radical. This results in the covalent attachment of nitrobenzene groups to the graphene lattice.[56,57]

3.2. Characterization of graphene reactivity

The reaction of graphene with 4-NBD induced the formation of sp^3-hybridized carbon within the graphene structure, which was detected by the emergence of the D peak in the corresponding Raman spectrum. Consequently, the ratio of the D peak intensity (I_D) to the G peak intensity (I_G), denoted as I_D/I_G, served as a quantitative measure of the extent of the reaction. The impact of strain on the reactivity of graphene can be evaluated by comparing the I_D/I_G ratio in the apex regions of the G/NS sample, where tensile strain is present, with that in the free-standing regions, where minimal or no strain is expected. To achieve this, Raman mapping of the G/NS samples was conducted. A laser beam of 532 nm wavelength was focused on the apex regions of the G/NS sample. Due to a height difference of 25 nm between the apex regions and the free-standing regions, the intensity of the SiO_2 peak (I_{SiO_2}) at approximately 464 cm^{-1} was higher in the apex regions, where the laser beam was well-focused, and lower in the free-standing regions, where the laser beam was less focused. Fig. 2a presents the intensity map of the SiO_2 peak, where the expected periodic pattern of the NS-array is clearly visible, enabling precise localization of the apex regions in the Raman maps. Fig. 2b shows the corresponding I_D/I_G maps for the same region. Using the I_{SiO_2} map, the Raman spectra of graphene, for the apex and free-standing regions, were separately averaged (Fig. 2c). Histograms of the I_D/I_G ratios for these two regions were also generated (Fig. 2d). The results clearly demonstrated that the I_D/I_G ratio was lower in the apex regions, where significant tensile strain was expected. The average I_D/I_G ratio was 0.4 and 0.5 in the apex and free-standing regions, respectively. This implies that the electrochemical reactivity of tensile-strained graphene may be lower than that of unstrained graphene, an observation that has not been reported previously and may indicate a new feature of the electrochemical behavior of tensile-strained graphene.

The spatial variations in the I_D/I_G ratio could be attributed to spatial variations in the doping levels barring variations in the defect density in graphene.[58] However, the average ratio of the 2D peak intensity to the G peak intensity (I_{2D}/I_G), which is highly sensitive to the doping level in graphene[59] was the same for the apex and free-standing regions (Fig. S3†). As such, the observed differences in the I_D/I_G ratios were not due to variations in doping between the two regions.

To eliminate any potential influence of topography or doping on the Raman analysis following the reaction, we transferred the reacted G/NS samples onto a flat wafer substrate by chemically etching the nanospheres.[60] SEM image of the transferred graphene revealed a distinctive wrinkle pattern originating from the etched nanosphere arrays (Fig. 2e). Upon removal of the nanosphere array, the graphene regions, initially suspended between the nanospheres, made contact with the flat substrate. The delaminated graphene regions retained the curvature imparted by the template (Fig. 2f, left). These curved regions were drawn down to the substrate by van der Waals interactions. This pre-existing curvature prevented perfect conformity to a flat surface, driving a morphological transformation that maximized the contact area with the substrate. This resulted in
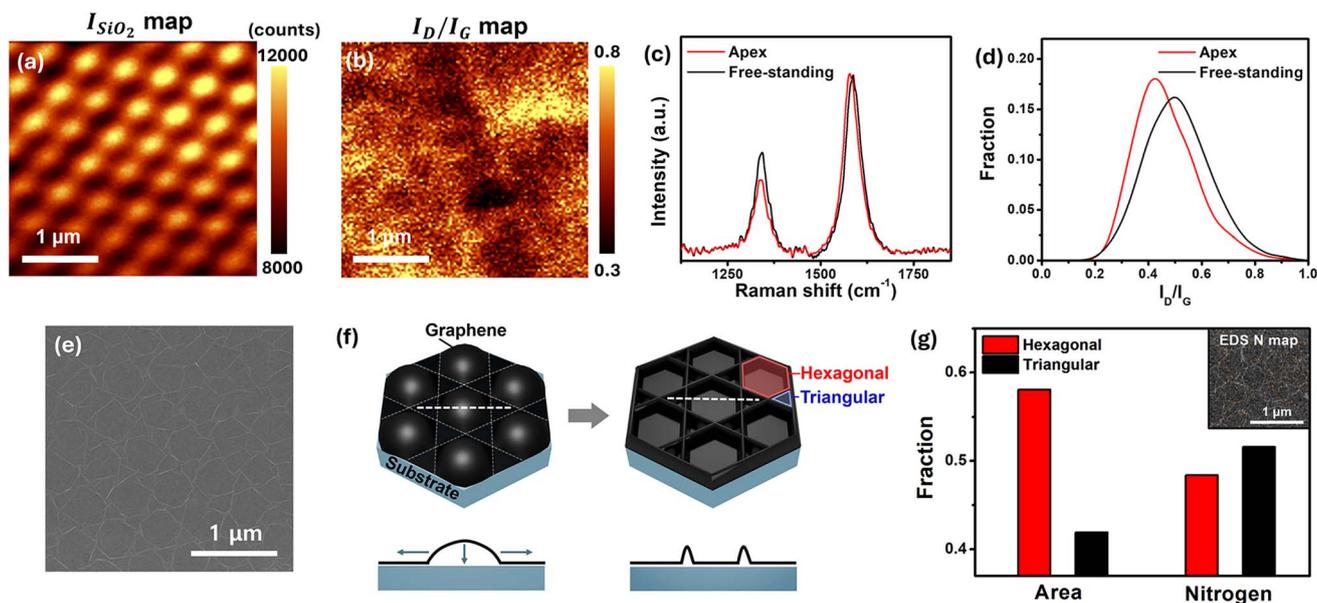
23698 | J. Mater. Chem. A, 2025, 13, 23696–23705

This journal is © The Royal Society of Chemistry 2025

Fig. 2 Raman and SEM analysis of graphene in the apex and free-standing regions of G/NS after reaction. Raman spatial maps showing (a) the SiO$_2$ peak intensity and (b) the I_D/I_G intensity ratio. (c) Average Raman spectra and (d) histograms of I_D/I_G ratios for the apex regions (red) and free-standing regions of G/NS (black). (e) SEM image of graphene transferred from G/NS to a flat wafer substrate after reaction with 4-NBD. (f) Schematic illustrating the formation of wrinkles in graphene during the removal of NS on a flat substrate. (g) Histograms of the EDS analysis showing the areal fraction and nitrogen count fractions for the hexagonal regions (red) and triangular regions (black). Inset: SEM image overlapped with the EDS map of nitrogen (orange dots).

the network of distinct wrinkles exhibiting characteristic hexagonal and triangular patterns (Fig. 2f, right), directly reflecting the symmetry of the original nanosphere array. Notably, no charging effects were observed in the SEM images. Charging effects resulting from electron accumulation or depletion on non-conductive or poorly conductive surfaces typically manifest as bright or dark artifacts. Upon the reaction of graphene with 4-NBD molecules, the generation of sp^3-hybridized C atoms significantly changed the electrical conductivity of the reacted graphene regions, resulting in charging effects.[60] Their absence in the former NS-contacted regions strongly suggests that the reaction did not occur to a greater extent in these areas.

Because the nitro group in the 4-NBD molecules contains nitrogen, the reacted regions of graphene can be identified by the presence of N atoms. Therefore, we obtained an energy-dispersive X-ray spectroscopy (EDS) map of N (Fig. 2g). A comparison of the integrated N signal intensity of the hexagonal regions (the centers of which were formerly NS-contacted regions) with that of the triangular regions (formerly free-standing regions) revealed that the hexagonal regions exhibited a 48% N signal fraction, which was less than their 58% areal fraction. This supports our hypothesis that the electrochemical reactivity of the tensile-strained graphene is lower than that of the unstrained graphene.

The electrochemical reaction between graphene and diazonium compounds is influenced by various factors, including mechanical strain,[44] shifts in the Fermi level due to doping,[37] and the amplitude of electron-hole puddles in graphene.[38] To isolate and investigate the effect of strain on the

electrochemical reactivity of graphene, comparing the reactivity across graphene samples subjected to different levels of strain while maintaining consistent doping levels and similar electron-hole puddle amplitudes is crucial. As the results shown in Fig. 2 are limited to a specific strain level in graphene, we prepared many G/NS samples to explore the effects of a wider range of strains on the reactivity of graphene. Additionally, we prepared a separate set of heavily p-doped graphene samples using an underside doping method,[61] in which bis(trifluoromethanesulfonyl)amide (TFSA) molecules were intercalated between graphene and the NS array (G/TFSA/NS). The G/TFSA/NS samples also met the aforementioned conditions.

To quantify the doping level, strain level, and amplitude of the electron-hole puddles in the G/NS and G/TFSA/NS samples, we employed Raman spectroscopy. Both the G and 2D peaks were fitted with Lorentzian line shapes, and the center positions of the G (ω_G) and 2D peaks (ω_{2D}), and the full width at half maximum (FWHM) of the 2D peaks (Γ_{2D}) were obtained for each set of graphene samples. Fig. 3a shows the (ω_G, ω_{2D}) data plotted in the $\omega_G - \omega_{2D}$ space for the two sets of samples. The doping and strain levels in the graphene were separated using Lee's method.[52] The amplitudes of the electron-hole puddles were estimated according to the formula $\alpha(\Gamma_{2D} - \Gamma_{2D}^0)$, where $\alpha = 0.08$ eV and $\Gamma_{2D}^0 = 26$ cm^{-1} is the 2D FWHM of graphene without electron-hole puddles.[38]

Consequently, the G/TFSA/NS samples exhibited a higher average hole concentration of 8.9×10^{12} cm^{-2} compared to an average hole concentration of 6.3×10^{12} cm^{-2} for the G/NS samples (Fig. 3b). Additionally, the G/TFSA/NS exhibited a higher average amplitude of the electron-hole puddles of
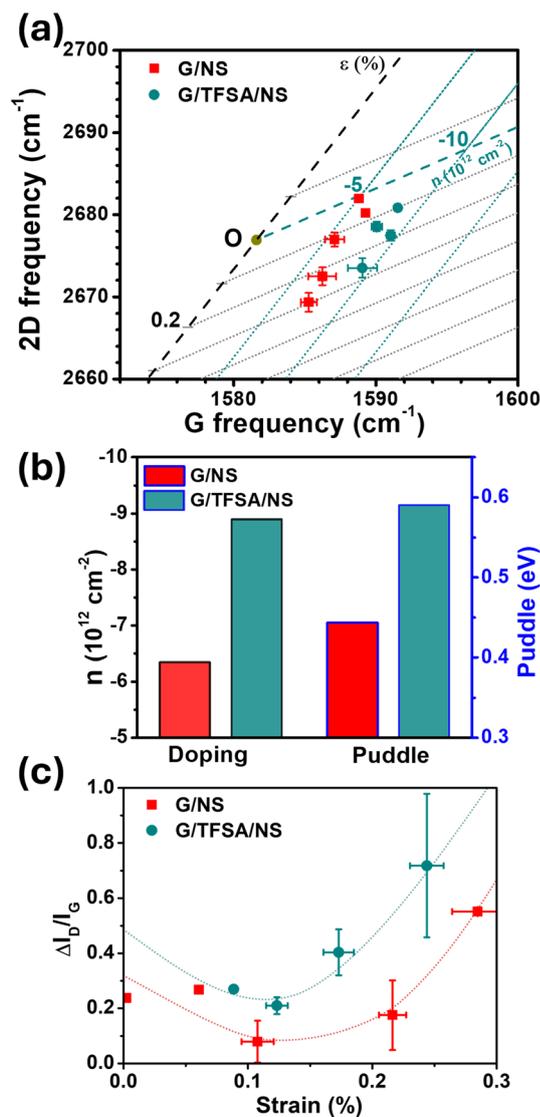
Fig. 3 Quantification of strain and doping levels in graphene on NS and their reactivity with 4-NBD. (a) Positions of the G and 2D peaks (ω_G, ω_{2D}) of G/NS (red squares) and G/TFSA/NS samples (green circles). (b) Histogram of average hole doping concentration (left) and the amplitude of electron–hole puddle (right) for G/NS (red bar) and G/TFSA/NS (green bar). (c) Change in I_D/I_G ratio ($\Delta I_D/I_G$) after diazonium functionalization as a function of strain for G/NS and G/TFSA/NS.

0.59 eV, as opposed to 0.44 eV in the G/NS samples. This increase in the amplitude of the electron–hole puddles in the G/TFSA/NS samples can be attributed to the spatially non-uniform distribution of the chemical dopant. Although the doping levels were comparable within the G/TFSA/NS and G/NS sample sets, the strain levels exhibited sample-to-sample variations ranging from 0% to 0.3%.

Notably, the laser beam size used in the Raman analysis was approximately 600 nm. This was larger than the diameter of the NS. Therefore, the Raman spectra represented the average of both the strained apex regions and the unstrained freestanding regions of G/NS. Consequently, the actual strain applied to the apex region of G/NS was much greater than the strain levels

estimated by Raman spectroscopy. Furthermore, the area of the strained regions was much smaller than that of the unstrained regions,[62] leading to the strain estimated from Raman spectroscopy being further reduced compared to the actual strain in the apex region of G/NS.[48,55]

The samples with varying strains were reacted with 4-NBD for 300 s to assess their electrochemical reactivity. The change in the I_D/I_G ratios of the samples before and after the reaction ($\Delta I_D/I_G$), as a function of strain, are plotted in Fig. 3c. At similar strain levels, $\Delta I_D/I_G$ for the G/TFSA/NS samples was higher than that for the G/NS samples, which could be attributed to the larger amplitude of electron–hole puddles in the G/TFSA/NS samples, consistent with previous studies.[38] We also noted that as strain increases, the $\Delta I_D/I_G$ initially decreases, but then increases around a strain of 0.1%. This observation differs from an earlier report on the strain-dependent reactivity of graphene, in which a continuous increase in the I_D/I_G ratio was observed with increasing strain.[44] In this previous study, the 4-NBD molecules primarily reacted at the defect sites in graphene, where the activation energy for the reaction can be inferred to have decreased with increasing strain. The discrepancy between our findings and those of previous reports may stem from differences in the initial defect densities of the graphene samples.

To confirm the general applicability of our findings, we extended our investigation to include another diazonium derivative, 4-methoxybenzenediazonium (4-MBD) (Fig. S4†). The electrochemical reactivity of graphene toward 4-MBD exhibited a similar non-monotonic dependence on tensile strain, characterized by an initial decrease in reactivity at lower strain levels followed by an increase at higher strains. This trend aligns closely with our observations for 4-NBD, validating that the observed strain-dependent electrochemical behavior is not specific to a single diazonium compound.

3.3. DFT calculations for graphene adsorption

Next, we researched to find a theoretical explanation for our experimental results. The coupling of a 4-NBD molecule with a graphene surface occurs *via* the following steps (Fig. 4a).[63–65] Initially, the solvated diazonium cation in aqueous solution is adsorbed onto the graphene surface (Step 1). The adsorption and desorption of diazonium cations occur rapidly on the graphene surface, and quasi-equilibrium between the concentration of desorbed diazonium ions and that of adsorbed diazonium ions on graphene is achieved. Upon electron transfer from graphene to the adsorbed 4-NBD molecule, nitrogen gas is released, resulting in the formation of a nitrophenyl radical (Step 2). Step 2 is the rate-limiting step,[63,65] and its reaction rate is formulated as,

$$\frac{d\sigma}{dt} = k_{ET}[D]_{ads}\left(1 - \frac{\sigma}{\rho_c}\right) \quad (1)$$

where k_{ET} is the rate constant for this electron transfer, $[D]_{ads}$ is the concentration of adsorbed diazonium ions on graphene, σ is the number density of reacted lattice sites, ρ_c is the number density of carbon atoms in graphene, and t is the reaction time.
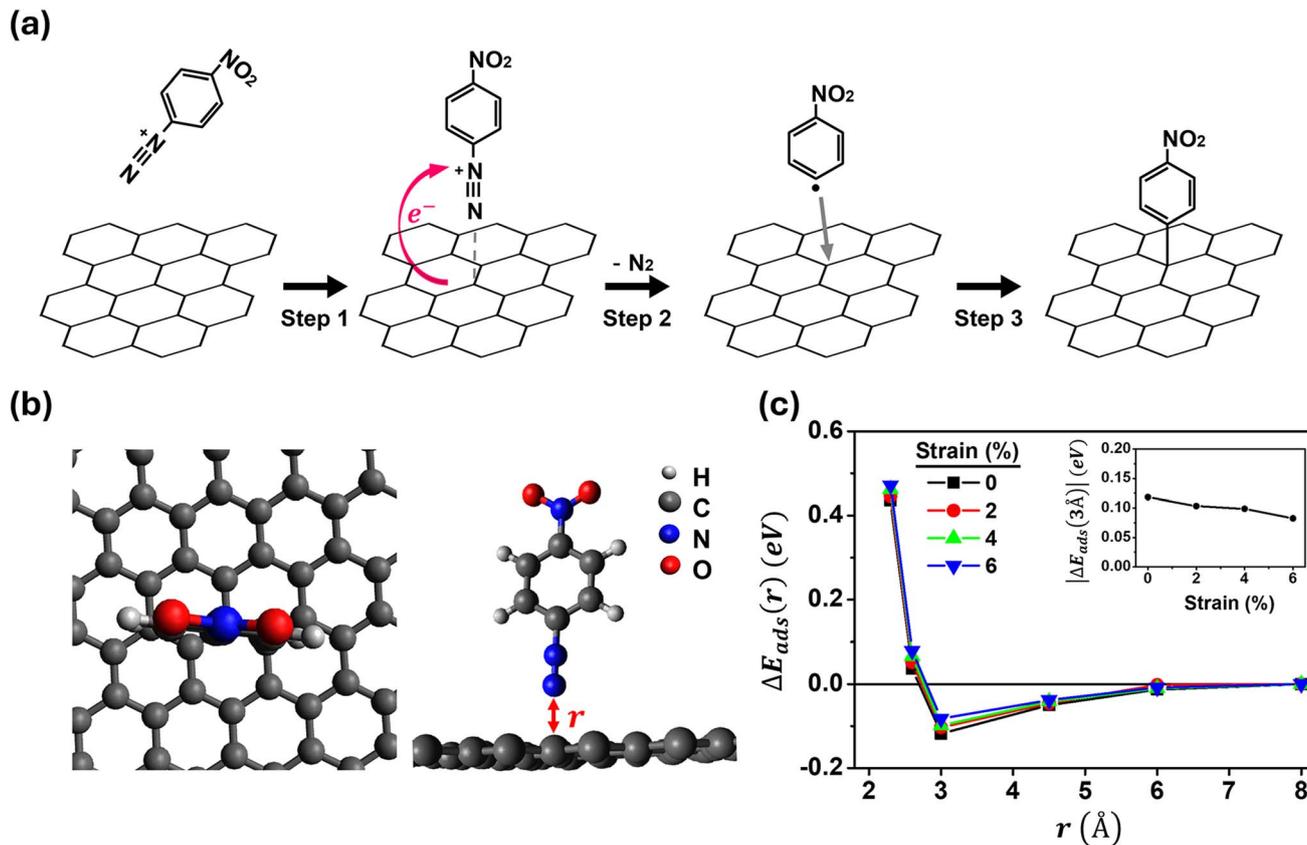
23700 | *J. Mater. Chem. A*, 2025, **13**, 23696–23705

This journal is © The Royal Society of Chemistry 2025

Fig. 4 DFT calculations on the adsorption of 4-NBD on graphene. (a) Schematic of the three-step coupling reaction between 4-NBD cation and graphene. Step 1: Adsorption of the diazonium cation onto graphene. Step 2: Electron transfer from graphene to 4-NBD leading to N_2 release and nitrophenyl radical formation. Step 3: Reaction of the nitrophenyl radical with an sp^2-carbon atom in the graphene lattice. (b) Top (left) and side (right) views of the molecular structure showing the adsorption configuration of 4-NBD and graphene. (c) ΔE_{ads} as a function of the distance r between 4-NBD and graphene under various strain conditions. Inset: $|\Delta E_{ads}|$ as a function of strain for $r = 3$ Å.

Eqn (1) shows that the strain in graphene can affect its reactivity by modulating either k_{ET} or $[D]_{ads}$. Lastly, the resulting nitrophenyl radical rapidly reacts with the sp^2-hybridized carbon atom in the graphene lattice (Step 3).

Our initial investigation aimed to determine whether the strain in graphene affects the adsorption behavior of 4-NBD cations, and thus, $[D]_{ads}$. For this purpose, we calculated the binding energies of the 4-NBD cations on graphene under various tensile strains using density functional theory (DFT) calculations (Fig. 4b, see Fig. S5† and Methods for more details). After individual optimizations of graphene and 4-NBD, the adsorption energy, E_{ads}, was calculated by evaluating the energy of the combined system at various distances between the optimized graphene and 4-NBD structures. The initial adsorption geometry of 4-NBD on graphene was set to match that predicted in a previous study on the adsorption of 4-sulfobenzenediazonium on graphene.[66] $E_{ads}(r)$ represents the adsorption energy as a function of the distance r between graphene and 4-NBD and was computed using the equation $E_{ads}(r) = E_{(graphene+4\text{-}NBD)} - E_{(graphene)} - E_{(4\text{-}NBD)}$, where $E_{(graphene+4\text{-}NBD)}$ is the total energy of the system with 4-NBD adsorbed on graphene, $E_{(graphene)}$ is the energy of the isolated graphene layer, and $E_{(4\text{-}NBD)}$ is the energy of the isolated 4-NBD molecule. r refers to the vertical

separation between the 4-NBD molecule and the graphene surface. By calculating $E_{ads}(r)$ at various distances, we obtained a detailed energy profile that characterized the adsorption behavior of 4-NBD on graphene. $E_{ads}(r)$ nearly saturates at $r = 8$ Å, with the values of $E_{ads}(r = 8$ Å$)$ differing by less than 0.3%, regardless of the strain applied to graphene. Therefore, the adsorption energy of the 4-NBD molecule on graphene, $\Delta E_{ads}(r)$, was then estimated by calculating the difference in adsorption energy between the 4-NBD molecule at distance r from graphene and at 8 Å as, $\Delta E_{ads}(r) = E_{ads}(r) - E_{ads}(r = 8$ Å$)$. Fig. 4c shows $\Delta E_{ads}(r)$ for various strain levels in graphene. For all strain levels in graphene, the adsorption energy exhibits a minimum at $r \sim 3$ Å. Within the range of 3 Å $< r < 8$ Å, as the distance r decreases, $\Delta E_{ads}(r)$ becomes increasingly negative, indicating stronger adsorption. However, when $r < 3$ Å, $\Delta E_{ads}(r)$ rapidly increases due to repulsive interactions between the graphene and the 4-NBD cation. Therefore, the value of $\Delta E_{ads}(r)$ at $r = 3$ Å in our DFT calculation is closely related to the equilibrium between the concentration of non-adsorbed diazonium ions and that of adsorbed diazonium ions on graphene ($[D]_{ads}$). Despite the significant strain variation from 0% to 6%, the difference in $\Delta E_{ads}(r = 3$ Å$)$ between the unstrained (0%) and highly strained (6%) graphene remains small at 0.04 eV.

This journal is © The Royal Society of Chemistry 2025

J. Mater. Chem. A, 2025, **13**, 23696–23705 | **23701**

According to these results, $[D]_{ads}$ can be concluded to be almost unaffected by the strain in graphene.

3.4. Theoretical modeling of electrochemical reactivity

Subsequently, we investigated the effects of strain on the rate constant of electron transfer, k_{ET}, from graphene to 4-NBD (Fig. 5). The rate constant k_{ET} is well-described by the Marcus–Gerischer theory as,[67–69]

$$k_{ET}(E_F) = \nu_n \int_{E_{redox}}^{E_F} \varepsilon_{red}(E) \, \mathrm{DOS}_G(E) \, W_{OX}(E) \, \mathrm{d}E \qquad (2)$$

where E_F is the Fermi level of graphene, $E_{redox} = -5.15$ eV is the standard potential of the redox couple of the 4-NBD diazonium salt, $\mathrm{DOS}_G(E)$ is the electronic density of states of graphene, and $W_{OX}(E)$ is the distribution of oxidized states of the solvated diazonium molecule. Here, $\nu_n \, \varepsilon_{red}(E) = 0.078$ eV s^{-1} is used to calculate k_{ET}.[38] The Fermi level E_F is

$$E_F = E_{D,0} + \mathrm{sgn}(n)\hbar\nu_F\sqrt{\pi|n|} \qquad (3)$$

where $E_{D,0}$ is the Dirac point energy of unstrained and undoped graphene (-4.4 eV),[70] ν_F is the Fermi velocity of graphene, $\mathrm{sgn}(n)$ is the sign function, and n is the charge carrier concentration (positive for electrons and negative for holes). $W_{OX}(E)$ is given by,

$$W_{OX}(E) = \frac{1}{\sqrt{4\pi\lambda kT}} \exp\left(-\frac{(E-(E_{redox}+\lambda))^2}{4\lambda kT}\right) \qquad (4)$$

where k is the Boltzmann constant, T is the absolute temperature, and $\lambda = 0.7$ eV (ref. 71) is the reorganization energy.

The electronic density of states of graphene ($\mathrm{DOS}_G(E)$) is,

$$\mathrm{DOS}_G(E) = \frac{2A_C|E - E_D|}{\pi\hbar^2\nu_F^2} \qquad (5)$$

where $A_C = 5.2 \times 10^{-16}$ cm^2 is the unit cell area of graphene and E_D is the Dirac point energy of graphene. Under mechanical strain ε, strain-field in graphene generates pseudo-electric fields. Consequently, E_D is shifted and $E_D = E_{D,0} - 2g_e\varepsilon$ where $g_e \approx 3.8$ eV.[41,43] Therefore, the presence of mechanical strain ε in graphene shifts the density of states $\mathrm{DOS}_G(E)$ due to the
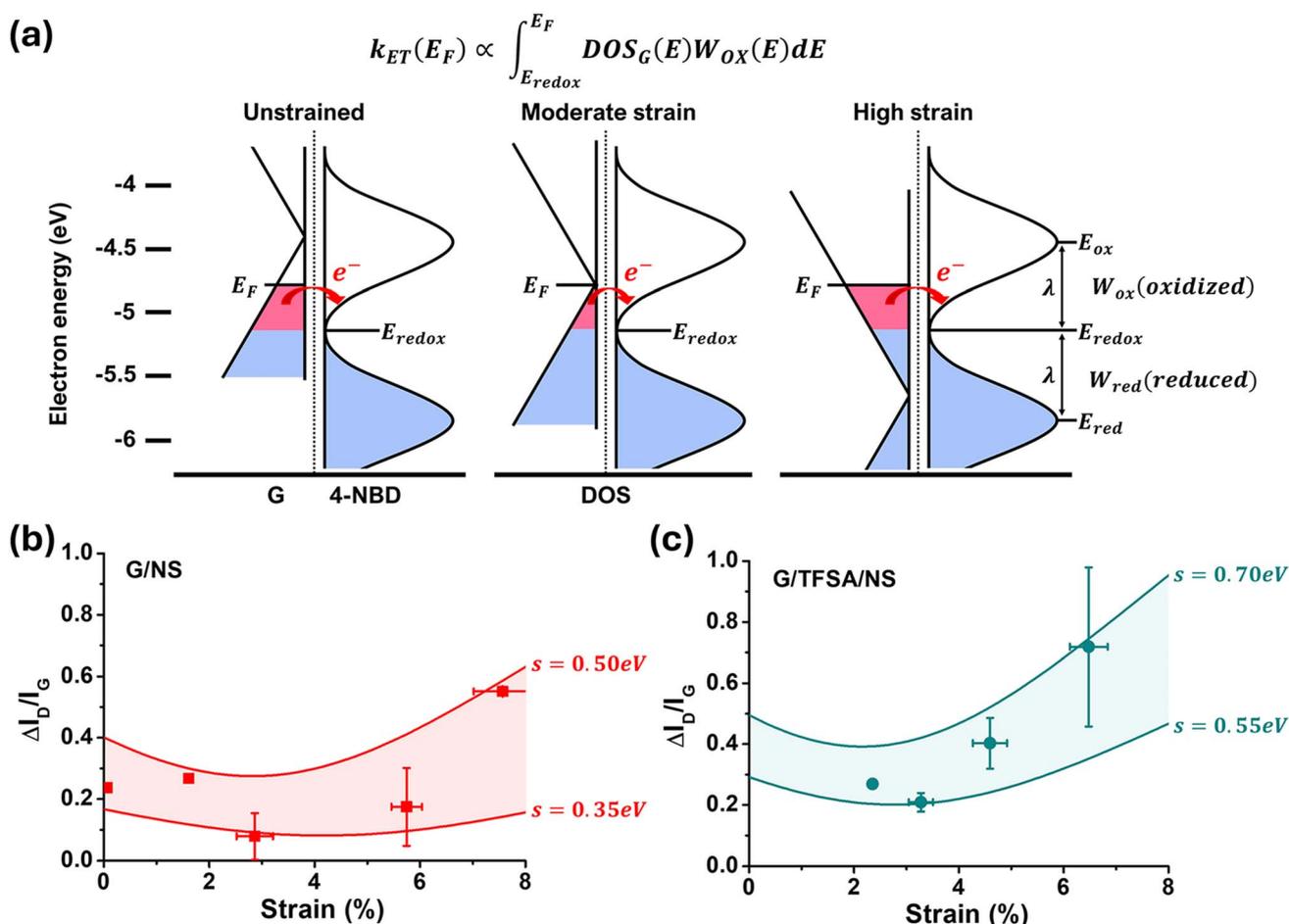

Fig. 5 Modified Marcus–Gerischer Theory. (a) Alignment of the density of states (DOS) of graphene ($\mathrm{DOS}_G(E)$) against the distribution of redox states $W_{OX}(E)$ and $W_{red}(E)$ of 4-NBD for unstrained (left), moderately strained (middle), and highly strained (right) graphene. The arrow indicates the direction of the electron transfer. (b) Calculated I_D/I_G as a function of strain for G/NS and (c) G/TFSA/NS. The S values are set to range from 0.35 to 0.50 eV for G/NS and from 0.55 to 0.70 eV for G/TFSA/NS, respectively. The scatter points represent experimental data from Fig. 3c, with the strain levels rescaled to account for the actual strain applied in the graphene regions directly adhered to NSs.

corresponding shift in the E_D. According to the Marcus–Gerischer theory (eqn (2)), this shift in $DOS_G(E)$ inevitably alters $k_{ET}(E_F)$. We propose that this alteration may be the underlying mechanism driving the effects of strain on the reactivity of defect-free graphene (Fig. 5a).

The presence of charged impurities near graphene creates electron–hole puddles, leading to charge fluctuations that affect the electron transfer rate from graphene to 4-NBD. To account for these fluctuations, we modified the Marcus–Gerischer theory by incorporating the spatial variation in the local Fermi level in graphene. In the presence of electron–hole puddles, the experimentally observed rate constant, $k_{ET,meas}$, is the average value of $k_{ET}(E_F)$ where E_F has a distribution centered around a certain average Fermi level, $E_{F,avg}$. Assuming that the Fermi level distribution is Gaussian with a mean value of $E_{F,avg}$ and a standard deviation of S, which represents the amplitude of the electron–hole puddles and denoted as $G(E_F; E_{F,avg}, S)$, the measured rate constant $k_{ET,meas}$ is calculated as follows:

$$k_{ET,meas} = \int_{E_{redox}}^{\infty} G(E_F; E_{F,avg}, S) k_{ET}(E_F) dE_F. \quad (6)$$

The independent parameters related graphene properties in this model are the charge carrier concentration n, the amplitude of the electron–hole puddles S, and the strain ε.

Finally, to correlate the model with the experimental data, specifically the I_D/I_G ratio as a function of reaction time t in this case, we performed the following series of calculations. In a first-order electron–transfer reaction model for Step 2 of the coupling of 4-NBD (eqn (1)), the average density of reacted lattice sites σ as a function of reaction time t is,

$$\sigma(t) = \rho_c (1 - \exp(-(k_{ET,meas}[D]_{ads}/\rho_c)t)). \quad (7)$$

Here, $[D]_{ads}$ was assumed to be constant according to the DFT calculation results (Fig. 4). Following the methodology outlined in previous studies, the density of reacted sites $\sigma(t)$ was then quantitatively correlated with I_D/I_G.[72]

Using eqn (1)–(7), we calculated the $I_D/I_G(t)$ as a function of ε at $t = 300$ s. As discussed, the actual strain applied to graphene at the apex of the G/NS or G/TFSA/NS samples was much larger than the strain estimated using Raman spectroscopy. Therefore, the simulation was conducted over a strain range of 0–8% rather than 0–0.3%, which is the range of the experimental strain obtained by Raman spectroscopy. To simulate the behaviors of the G/NS and G/TFSA/NS samples, we set the values of n and S according to the experimental data shown in Fig. 3b. For G/NS samples, n was set to -6.3×10^{12} cm^{-2} and S ranged from 0.35 to 0.50 eV. For G/TFSA/NS samples, n was set to -8.9×10^{12} cm^{-2} and S ranged from 0.55 to 0.70 eV. Fig. 5b and c show the simulated I_D/I_G as a function of ε at $t = 300$ s for G/NS sample and G/TFSA/NS samples, respectively. Consequently, the simulation predicts that I_D/I_G is larger when the amplitude of the electron–hole puddle, represented by S in this model, is greater, which is consistent with previous reports and our experimental observations. More importantly, the simulations reveal that I_D/I_G decreases with increasing strain ε up to

a certain level. After the strain exceeds this level, I_D/I_G begins to increase. This simulated trend is consistent with the experimental results presented in Fig. 3. Moreover, the experimental I_D/I_G values as a function of ε (Fig. 3c) align with the simulation results (Fig. 5b and c) when the strain values estimated by Raman spectroscopy are appropriately rescaled. Here, we note that although the theoretical model captures the qualitative trends accurately, its quantitative predictive capability is limited due to inherent uncertainties associated with key graphene parameters, such as the Fermi velocity and the amplitude of electron–hole puddles.

4. Conclusions

In conclusion, we explored the impact of mechanical strain on the electrochemical reactivity of graphene with 4-NBD by combining experimental techniques and theoretical modeling. Our results demonstrate that the electrochemical reactivity of graphene exhibits a nonlinear response to mechanical strain: it initially decreases with strain but increases as strain continues to rise. This intriguing behavior can be explained using Marcus–Gerischer theory, which accounts for the strain-induced shifts in the electronic density of states of graphene owing to the strain-induced pseudo-electric field and the corresponding impact on the electron transfer rate between graphene and 4-NBD. Our study provides new insights into the strain-dependent reactivity of graphene, emphasizing the need to consider both mechanical and electronic factors when designing graphene-based materials for electrochemical applications.

Data availability

The data supporting this article have been included as part of the ESI.†

Author contributions

Hyo Jin Lee: formal analysis, investigation, writing – original draft, writing – review & editing. Jinhyun Hwang: investigation. Hyo Chan Hong: investigation. Young Wook Hwang: investigation. Jiyeon Lee: investigation. Gaeun Cho: investigation. Dalsu Choi: investigation. Kilwon Cho: conceptualization, investigation, supervision, writing – original draft, writing – review & editing. Hyo Chan Lee: conceptualization, funding acquisition, investigation, supervision, writing – original draft, writing – review & editing.

Conflicts of interest

There are no conflicts to declare.

Acknowledgements

This journal is © The Royal Society of Chemistry 2025

J. Mater. Chem. A, 2025, 13, 23696–23705 | 23703

Notes and references

1 Y. Liu, X. Dong and P. Chen, *Chem. Soc. Rev.*, 2012, **41**, 2283–2307.

2 L. Feng, L. Wu and X. Qu, *Adv. Mater.*, 2013, **25**, 168–186.

3 Y. Yang, A. M. Asiri, Z. Tang, D. Du and Y. Lin, *Mater. Today*, 2013, **16**, 365–373.

4 M. Pumera, *Mater. Today*, 2011, **14**, 308–315.

5 C. Rao, A. Sood, K. Subrahmanyam and A. Govindaraj, *Angew. Chem., Int. Ed.*, 2009, **48**, 7752–7777.

6 W. Fu, L. Jiang, E. P. van Geest, L. M. Lima and G. F. Schneider, *Adv. Mater.*, 2017, **29**, 1603610.

7 C.-H. Kim and C. D. Frisbie, *J. Phys. Chem. C*, 2014, **118**, 21160–21169.

8 P. Kafle, S. Huang, K. S. Park, F. Zhang, H. Yu, C. E. Kasprzak, H. Kim, C. M. Schroeder, A. M. Van Der Zande and Y. Diao, *Langmuir*, 2022, **38**, 6984–6995.

9 S. Pecorario, A. D. Scaccabarozzi, D. Fazzi, E. Gutiérrez-Fernández, V. Vurro, L. Maserati, M. Jiang, T. Losi, B. Sun, R. R. Tykwinski, C. S. Casari and M. Caironi, *Adv. Mater.*, 2022, **34**, 2110468.

10 N. Mohanty and V. Berry, *Nano Lett.*, 2008, **8**, 4469–4476.

11 J. S. Lee, H.-A. Joung, M.-G. Kim and C. B. Park, *ACS Nano*, 2012, **6**, 2978–2983.

12 M. Xue, C. Mackin, W.-H. Weng, J. Zhu, Y. Luo, S.-X. L. Luo, A.-Y. Lu, M. Hempel, E. McVay, J. Kong and T. Palacios, *Nat. Commun.*, 2022, **13**, 5064.

13 M. Singh, M. Holzinger, M. Tabrizian, S. Winters, N. C. Berner, S. Cosnier and G. S. Duesberg, *J. Am. Chem. Soc.*, 2015, **137**, 2800–2803.

14 M. T. Hwang, M. Heiranian, Y. Kim, S. You, J. Leem, A. Taqieddin, V. Faramarzi, Y. Jing, I. Park, A. M. van der Zande, S. Nam, N. R. Aluru and R. Bashir, *Nat. Commun.*, 2020, **11**, 1543.

15 Y. Lee, J. Kwon, E. Hwang, C.-H. Ra, W. J. Yoo, J.-H. Ahn, J. H. Park and J. H. Cho, *Adv. Mater.*, 2014, **27**, 41–46.

16 C. Wetzl, A. Silvestri, M. Garrido, H. L. Hou, A. Criado and M. Prato, *Angew. Chem.*, 2023, **135**, e202212857.

17 D. Li, Y. Luo, D. Onidas, L. He, M. Jin, F. Gazeau, J. Pinson and C. Mangeney, *Adv. Colloid Interface Sci.*, 2021, **294**, 102479.

18 Y. Xia, L. Sun, S. Eyley, B. Daelemans, W. Thielemans, J. Seibel and S. De Feyter, *Adv. Sci.*, 2022, **9**, 2105017.

19 A. Kaplan, Z. Yuan, J. D. Benck, A. G. Rajan, X. S. Chu, Q. H. Wang and M. S. Strano, *Chem. Soc. Rev.*, 2017, **46**, 4530–4571.

20 G. Bottari, M. Á. Herranz, L. Wibmer, M. Volland, L. Rodríguez-Pérez, D. M. Guldi, A. Hirsch, N. Martín, F. D'Souza and T. Torres, *Chem. Soc. Rev.*, 2017, **46**, 4464–4500.

21 T. Kuila, S. Bose, A. K. Mishra, P. Khanra, N. H. Kim and J. H. Lee, *Prog. Mater. Sci.*, 2012, **57**, 1061–1105.

22 A. A. Mohamed, Z. Salmi, S. A. Dahoumane, A. Mekki, B. Carbonnier and M. M. Chehimi, *Adv. Colloid Interface Sci.*, 2015, **225**, 16–36.

23 Z. Qiu, J. Yu, P. Yan, Z. Wang, Q. Wan and N. Yang, *ACS Appl. Mater. Interfaces*, 2016, **8**, 28291–28298.

24 B. D. Assresahegn, T. Brousse and D. Bélanger, *Carbon*, 2015, **92**, 362–381.

25 S. Mahouche-Chergui, S. Gam-Derouich, C. Mangeney and M. M. Chehimi, *Chem. Soc. Rev.*, 2011, **40**, 4143–4166.

26 C. M. Bazán, A. Béraud, M. Nguyen, A. Bencherif, R. Martel and D. Bouilly, *Nano Lett.*, 2022, **22**, 2635–2642.

27 C. Cao, Y. Zhang, C. Jiang, M. Qi and G. Liu, *ACS Appl. Mater. Interfaces*, 2017, **9**, 5031–5049.

28 G. L. Paulus, Q. H. Wang and M. S. Strano, *Acc. Chem. Res.*, 2013, **46**, 160–170.

29 R. Sharma, J. H. Baik, C. J. Perera and M. S. Strano, *Nano Lett.*, 2010, **10**, 398–405.

30 D. Belanger and J. Pinson, *Chem. Soc. Rev.*, 2011, **40**, 3995–4048.

31 Z. Xia, F. Leonardi, M. Gobbi, Y. Liu, V. Bellani, A. Liscio, A. Kovtun, R. Li, X. Feng, E. Orgiu, P. Samorì, E. Treossi and V. Palermo, *ACS Nano*, 2016, **10**, 7125–7134.

32 J. Greenwood, T. H. Phan, Y. Fujita, Z. Li, O. Ivasenko, W. Vanderlinden, H. Van Gorp, W. Frederickx, G. Lu and K. Tahara, *ACS Nano*, 2015, **9**, 5520–5535.

33 C. Cheng, P. Jia, L. Xiao and J. Geng, *Carbon*, 2019, **145**, 668–676.

34 G. Abellán, M. Schirowski, K. F. Edelthalhammer, M. Fickert, K. Werbach, H. Peterlik, F. Hauke and A. Hirsch, *J. Am. Chem. Soc.*, 2017, **139**, 5175–5182.

35 B. D. Ossonon and D. Bélanger, *Carbon*, 2017, **111**, 83–93.

36 C.-J. Shih, Q. H. Wang, Z. Jin, G. L. Paulus, D. Blankschtein, P. Jarillo-Herrero and M. S. Strano, *Nano Lett.*, 2013, **13**, 809–817.

37 M. J. Park, H.-H. Choi, B. Park, J. Y. Lee, C.-H. Lee, Y. S. Choi, Y. Kim, J. M. Yoo, H. Lee and B. H. Hong, *Chem. Mater.*, 2018, **30**, 5602–5609.

38 Q. H. Wang, Z. Jin, K. K. Kim, A. J. Hilmer, G. L. Paulus, C.-J. Shih, M.-H. Ham, J. D. Sanchez-Yamagishi, K. Watanabe, T. Taniguchi, J. Kong, P. Jarillo-Herrero and M. S. Strano, *Nat. Chem.*, 2012, **4**, 724–732.

39 Y. Yu, K. Zhang, H. Parks, M. Babar, S. Carr, I. M. Craig, M. Van Winkle, A. Lyssenko, T. Taniguchi, K. Watanabe, V. Viswanathan and D. K. Bediako, *Nat. Chem.*, 2022, **14**, 267–273.

40 Y. Ding, Q. Peng, L. Gan, R. Wu, X. Ou, Q. Zhang and Z. Luo, *Chem. Mater.*, 2016, **28**, 1034–1039.

41 L. Wang, A. Baumgartner, P. Makk, S. Zihlmann, B. S. Varghese, D. I. Indolese, K. Watanabe, T. Taniguchi and C. Schönenberger, *Commun. Phys.*, 2021, **4**, 147.

42 S.-M. Choi, S.-H. Jhi and Y.-W. Son, *Phys. Rev. B:Condens. Matter Mater. Phys.*, 2010, **81**, 081407.

43 D. Grassano, M. D'Alessandro, O. Pulci, S. Sharapov, V. Gusynin and A. Varlamov, *Phys. Rev. B*, 2020, **101**, 245115.

44 M. A. Bissett, S. Konabe, S. Okada, M. Tsuji and H. Ago, *ACS Nano*, 2013, **7**, 10335–10343.

45 N. Hawthorne, S. Banerjee, Q. Moore, A. M. Rappe and J. D. Batteas, *J. Phys. Chem. C*, 2022, **126**, 17569–17578.

46 X. Fan, R. Nouchi and K. Tanigaki, *J. Phys. Chem. C*, 2011, **115**, 12960–12964.

23704 | *J. Mater. Chem. A*, 2025, **13**, 23696–23705

This journal is © The Royal Society of Chemistry 2025

47 Q. Wu, Y. Wu, Y. Hao, J. Geng, M. Charlton, S. Chen, Y. Ren, H. Ji, H. Li, D. W. Boukhvalov, R. D. Piner, C. W. Bielawski and R. S. Ruoff, *Chem. Commun.*, 2013, **49**, 677–679.

48 Y. Zhang, M. Heiranian, B. Janicek, Z. Budrikis, S. Zapperi, P. Y. Huang, H. T. Johnson, N. R. Aluru, J. W. Lyding and N. Mason, *Nano Lett.*, 2018, **18**, 2098–2104.

49 Y. Zhang, Y. Kim, M. J. Gilbert and N. Mason, *npj 2D Mater. Appl.*, 2018, **2**, 31.

50 Y. Zhang, Y. Kim, M. J. Gilbert and N. Mason, *Appl. Phys. Lett.*, 2019, **115**, 143508.

51 E. Hohlfeld and B. Davidovitch, *Phys. Rev. E:Stat., Nonlinear, Soft Matter Phys.*, 2015, **91**, 012407.

52 J. E. Lee, G. Ahn, J. Shim, Y. S. Lee and S. Ryu, *Nat. Commun.*, 2012, **3**, 1024.

53 J. Zabel, R. R. Nair, A. Ott, T. Georgiou, A. K. Geim, K. S. Novoselov and C. Casiraghi, *Nano Lett.*, 2012, **12**, 617–621.

54 M. Mohr, J. Maultzsch and C. Thomsen, *Phys. Rev. B:Condens. Matter Mater. Phys.*, 2010, **82**, 201409.

55 J. Hwang, J. Park, J. Choi, T. Lee, H. C. Lee and K. Cho, *Adv. Sci.*, 2024, **11**, 2400598.

56 J. Park and M. Yan, *Acc. Chem. Res.*, 2013, **46**, 181–189.

57 A. Criado, M. Melchionna, S. Marchesan and M. Prato, *Angew. Chem., Int. Ed.*, 2015, **54**, 10734–10750.

58 M. Bruna, A. K. Ott, M. Ijäs, D. Yoon, U. Sassi and A. C. Ferrari, *ACS Nano*, 2014, **8**, 7432–7441.

59 A. Das, S. Pisana, B. Chakraborty, S. Piscanec, S. K. Saha, U. V. Waghmare, K. S. Novoselov, H. R. Krishnamurthy, A. K. Geim, A. C. Ferrari and A. K. Sood, *Nat. Nanotechnol.*, 2008, **3**, 210–215.

60 L. Zhou, L. Liao, J. Wang, J. Yu, D. Li, Q. Xie, Z. Liu, Y. Yang, X. Guo and Z. Liu, *Adv. Mater.*, 2016, **28**, 2148–2154.

61 J. S. Kim, B. J. Kim, Y. J. Choi, M. H. Lee, M. S. Kang and J. H. Cho, *Adv. Mater.*, 2016, **28**, 4803–4810.

62 J. Varillas and O. Frank, *Carbon*, 2021, **173**, 301–310.

63 M. L. Usrey, E. S. Lippmann and M. S. Strano, *J. Am. Chem. Soc.*, 2005, **127**, 16129–16135.

64 L. R. Powell, Y. Piao, Y. Wang and J. Phy, *Chem. Lett.*, 2016, **7**, 3690–3694.

65 J. Hong, S. Niyogi, E. Bekyarova, M. E. Itkis, P. Ramesh, N. Amos, D. Litvinov, C. Berger, W. A. De Heer and S. Khizroev, *Small*, 2011, **7**, 1175–1180.

66 A. Dammak, F. Raouafi, A. Cavanna, P. Rudolf, D. Di Caprio, V. Sallet, A. Madouri and J.-M. Jancu, *RSC Adv.*, 2022, **12**, 36002–36011.

67 K.-W. Chang, I. A. Santos, Y. Nguyen, Y.-H. Su, C. C. Hsu, Y.-P. Hsieh and M. Hofmann, *Chem. Mater.*, 2018, **30**, 7178–7182.

68 P. L. Levesque, S. S. Sabri, C. M. Aguirre, J. Guillemette, M. Siaj, P. Desjardins, T. Szkopek and R. Martel, *Nano Lett.*, 2011, **11**, 132–137.

69 R. Sharma, N. Nair and M. S. Strano, *J. Phys. Chem. C*, 2009, **113**, 14771–14777.

70 J. M. Kim, S. Kim, D. H. Shin, S. W. Seo, H. S. Lee, J. H. Kim, C. W. Jang, S. S. Kang, S.-H. Choi, G. Y. Kwak, K. J. Kim, H. Lee and H. Lee, *Nano Energy*, 2018, **43**, 124–129.

71 N. Nair, W.-J. Kim, M. L. Usrey and M. S. Strano, *J. Am. Chem. Soc.*, 2007, **129**, 3946–3954.

72 M. M. Lucchese, F. Stavale, E. M. Ferreira, C. Vilani, M. V. d. O. Moutinho, R. B. Capaz, C. A. Achete and A. Jorio, *Carbon*, 2010, **48**, 1592–1597.

This journal is © The Royal Society of Chemistry 2025

J. Mater. Chem. A, 2025, **13**, 23696–23705 | **23705**